IDE∆L®

A Comparative Study of Acquisition Schemes
for Diffusion Tensor Imaging Using MRI

Nikolaos G. Papadakis, Da Xing, Christopher L.-H. Huang,* Laurance D. Hall, and T. Adrian Carpenter[1]

*Herchel Smith Laboratory for Medicinal Chemistry, University of Cambridge School of Clinical Medicine, University Forvie Site, Robinson Way, Cambridge CB2 2PZ, England, United Kingdom; and *Department of Physiology, University of Cambridge, Physiological Laboratory, Downing Street, Cambridge CB2 3EG, England, United Kingdom*

This study has investigated the effects of the selection of the diffusion-weighted (DW) gradient directions on the precision of a diffusion tensor imaging (DTI) experiment. The theoretical analysis provided a quantitative framework in which the noise performance of DTI schemes could be assessed objectively and for the development of novel DTI schemes, which employ multiple DW gradient directions. This generic framework was first applied to the examination of two commonly used DTI schemes, which employed 6 DW gradient directions and hitherto were used indiscriminately under the sole condition of noncollinearity. It was then used to design and assess a novel 12-DW-gradient-direction DTI protocol, which employed the same total number of DW acquisitions as the two conventional schemes (*12*). This theoretical investigation was then corroborated using rigorous simulation and DTI experiments on both an isotropic phantom and a healthy human brain. Both the theoretical and the experimental analysis demonstrated that the two conventional schemes showed a significantly different noise performance and that use of the new multiple-DW-gradient-direction scheme clearly improved the precision of the DTI measurements. © 1999 Academic Press

Key Words: magnetic resonance imaging; diffusion; tensor; anisotropy; noise; optimization.

INTRODUCTION

Diffusion tensor imaging (DTI) using magnetic resonance imaging (MRI) was recently proposed (*1, 2*) and has been used for the *in vivo* study of cerebral (*3, 4*), cardiac (*5*), and other tissues (*6, 7*), providing complete directional descriptions to be made of the self-diffusion properties of water through the tissue structure. DTI is therefore potentially useful not only for the characterization of the architecture of healthy tissues (*8, 9*) and their function (*10*), but also for diagnosis and assessment of disease conditions which perturb tissue structural coherence (such as acute stroke (*11, 12*), cerebral ischemia (*13*), multiple sclerosis (*14*), schizophrenia (*15*), gliosis (*16*), and tumor growth in the brain (*17*)).

DTI acquisition and processing schemes entail two overall steps (*2*): (a) First, a series of diffusion-weighted (DW) signals are acquired using DW gradients that vary both in magnitude and direction; these signals are used for the determination of the six independent elements of the symmetric 3×3 diffusion tensor **D**. (b) Second, rotationally invariant scalar quantities which describe the intrinsic diffusion properties are calculated from **D**. These include the three principal diffusivities (*1*), which are the eigenvalues of **D**, the mean value of the trace of **D**, and the anisotropy indices (*8, 18*). Maps of such rotationally invariant scalars are the important "end-results" of DTI.

The precision in the final results of DTI measurements depends on the noise propagation from the initially acquired DW signals through both these steps. Clearly, an efficient DTI acquisition and processing scheme should minimize noise propagation at each individual step. However, there has been no systematic study of the error propagation through the DTI acquisition schemes that were used in step (a). The available published DTI data have always been acquired from schemes that used several (six (*3–6*) or seven (*1, 7, 19*)) noncollinear DW directions. Two sets of six DW directions have been arbitrarily proposed and used indiscriminately on the basis of their noncollinearity (*3, 4*) alone. Adding one more DW gradient direction to one of those schemes has yielded a seven-DW-direction scheme (*1*), which has also been used in some DTI experiments.

This paper addresses the problem of error propagation in the aforementioned step (a), as well as the effect of the selection of specific DW gradient directions on measurement precision. The analysis begins from the elementary equations characterizing generalized DTI acquisition schemes; it then defines a quantitative index which evaluates the effect of the DW gradient directions of a DTI scheme on the performance of the scheme as reflected in the precision of the measurements. This index was then used to evaluate two commonly used DTI schemes and to develop new DTI schemes. Finally, the validity of the index and the performance of the new and the currently used schemes were tested using computer simulations and DTI experiments in a phantom and in a healthy human brain.

THEORY

Definition of an Index for a DTI Acquisition Scheme

It is well known that the incorporation of a DW gradient pair in a spin-echo experiment makes it possible to extract infor-

mation about the self-diffusion tensor $\mathbf{D}$ (1, 2, 20). In the presence of such a DW gradient pair, for which the DW gradient is described by the vector $\mathbf{G}_D = [G_{Dx}G_{Dy}G_{Dz}]^T = G_{Dm}[g_{Dx}g_{Dy}g_{Dz}]^T = G_D\mathbf{g}_D$ (G_{Dm} is the magnitude of the DW gradient, $\mathbf{g}_D = [g_{Dx}g_{Dy}g_{Dz}]^T$ is the unity vector describing its direction, and ^{T} denotes the transpose), and ignoring the effects of the imaging gradients, the DW pixel intensity S is

$$S = S_0\exp(-B\mathbf{g}_D^T \cdot \mathbf{D} \cdot \mathbf{g}_D), \qquad [1]$$

where S_0 is the baseline pixel intensity in the absence of any DW gradient, $\mathbf{D}$ is the (apparent) diffusion tensor,

$$\mathbf{D} = \begin{bmatrix} D_{xx} & D_{xy} & D_{xz} \\ D_{xy} & D_{yy} & D_{yz} \\ D_{xz} & D_{yz} & D_{zz} \end{bmatrix},$$

and B is the scalar b factor (or b value) (20, 21), which depends only on the magnitude of the DW gradient (as distinct from its direction), the duration, the temporal spacing, and the shape of the DW gradient pulses. For example, for rectangular DW gradient pulses of duration δ and temporal spacing Δ, $B = \gamma^2\delta^2(\Delta - \delta/3)G_{Dm}^2$ (γ is the gyromagnetic ratio).

Defining the six-dimensional (6D) vectors

$$\mathbf{d} = [d_1d_2d_3d_4d_5d_6]^T = [D_{xx}D_{yy}D_{zz}D_{xy}D_{xz}D_{yz}]^T,$$
$$\mathbf{b} = [g_{Dx}^2g_{Dy}^2g_{Dz}^2 2g_{Dx}g_{Dy}2g_{Dx}g_{Dz}2g_{Dy}g_{Dz}]^T, \qquad [2]$$

we have

$$S = S_0\exp(-B\mathbf{b}^T\mathbf{d}), \quad \mathbf{b}^T\mathbf{d} = \frac{1}{B}\ln\left(\frac{S_0}{S}\right). \qquad [3]$$

Provided that the baseline image S_0 is known from a separate measurement with the DW gradients set equal to zero, Eq. [3] is a linear equation whose unknowns are the six elements of $\mathbf{d}$, which are the six independent elements of the diffusion tensor $\mathbf{D}$.

Acquisition of N DW images, with the ith image having signal intensity S_i, and corresponding to the DW gradient direction $\mathbf{g}_i = [g_{ix}g_{iy}g_{iz}]^T$, the b vector $\mathbf{b}_i = [b_{i1}b_{i2}b_{i3}b_{i4}b_{i5}b_{i6}]^T$ and the b value B_i ($i = 1, \ldots, N$), produces the following system of N linear equations with six unknowns,

$$\mathscr{B}\mathbf{d} = \mathbf{C}, \qquad [4]$$

where the $N \times 6$ matrix $\mathscr{B}$ of the gradient directions of the DTI acquisition scheme is defined as: $\mathscr{B}^T = [\mathbf{b}_1 \ldots \mathbf{b}_N]$, and the N-dimensional vector $\mathbf{C}$ contains the signals corresponding to the N DW acquisitions, $\mathbf{C} = [1/B_1\ln(S_0/S_1) \ldots 1/B_N\ln(S_0/S_N)]^T$.

Stable and robust determination of the diffusion tensor elements in the presence of noise requires that the number N of the acquired DW signals, and therefore the number of the equations of the linear system of Eq. [4], is larger than the number of the unknowns (i.e., the six elements of the diffusion tensor). Accordingly, $N > 6$, and the overdetermined system of Eq. [4] can be solved by singular value decomposition (SVD) (22) of $\mathscr{B}$ so that $\mathscr{B} = \mathbf{U}\mathbf{W}\mathbf{V}^T$, where $\mathbf{U}$ is an $N \times 6$ column-orthonormal matrix and $\mathbf{V}$ is a 6×6 orthonormal matrix. The matrix $\mathbf{W}$ is a 6×6 diagonal matrix with elements w_i, ($i = 1, \ldots, 6$), which are nonzero, if the linear system of Eq. [4] contains at least six independent equations. This requires that at least six noncollinear DW gradient directions with independent $\mathbf{b}$ vectors are employed for the acquisition of the N DW images. Therefore, the pseudo-inverse $\mathscr{B}^{-1}$ is $\mathscr{B}^{-1} = \mathscr{A} = \mathbf{V}\mathbf{W}^{-1}\mathbf{U}^T$, and the elements of $\mathbf{D}$ can be calculated from the equation

$$\mathbf{d} = \mathscr{B}^{-1}\mathbf{C} = \mathscr{A}\mathbf{C}.$$

The error $\delta\mathbf{C}$ of the vector $\mathbf{C}$ of the DW signals is transformed into the error $\delta\mathbf{d}$ of the vector $\mathbf{d}$ of the diffusion tensor elements, as follows:

$$\delta\mathbf{d} = \mathscr{A}\delta\mathbf{C}$$
$$\delta\mathbf{d}\delta\mathbf{d}^T = \mathscr{A}\delta\mathbf{C}\delta\mathbf{C}^T\mathscr{A}^T$$
$$\mathbf{E} = \langle\delta\mathbf{d}\delta\mathbf{d}^T\rangle = \mathscr{A}\langle\delta\mathbf{C}\delta\mathbf{C}^T\rangle\mathscr{A}^T, \qquad [5]$$

where $\langle\ \rangle$ denotes statistical mean value.

The covariance matrix (23) $\langle\delta\mathbf{C}\delta\mathbf{C}^T\rangle$ of the errors in $\mathbf{C}$ is transformed to the covariance matrix $\mathbf{E}$ of the errors in $\mathbf{d}$ via the matrix $\mathscr{A}$ and its transpose. However, the matrix $\langle\delta\mathbf{C}\delta\mathbf{C}^T\rangle$ and therefore the matrix $\mathbf{E}$ depends additionally on the b values used by the DTI acquisition scheme and also on the specific form of the diffusion tensor $\mathbf{D}$. Because the present analysis investigates the effect of the DW gradient directions on the DTI schemes, Eq. [5] can reflect only that effect by assuming that the errors in $\mathbf{C}$ are uncorrelated and have equal variances σ^2, so that $\langle\delta\mathbf{C}\delta\mathbf{C}^T\rangle = \sigma^2\mathbf{I}$, where $\mathbf{I}$ is the $N \times N$ unity matrix. Equation [5] then becomes

$$\mathbf{E} = \sigma^2\mathscr{A}\mathscr{A}^T = \sigma^2\mathbf{F},$$

where $\mathbf{F} = \mathscr{A}\mathscr{A}^T$.

The diagonal elements of $\mathbf{E}$ give the variance of the respective tensor elements of $\mathbf{d}$ (23), while $\mathbf{F}$ describes the propagation of the uncorrelated errors in the elements of $\mathbf{C}$ to errors in the tensor elements, and depends exclusively on the employed DW gradient directions. The total variance σ_D^2 of the measured tensor $\mathbf{D}$, defined as the sum of the variances of its individual elements, can be used as a quantitative indicator of the total

error in the measurement of **D**. Because the off-diagonal elements of **D** appear twice in its expression, their variances contribute twice in $\sigma_\mathbf{D}^2$. We then have

$$\sigma_\mathbf{D}^2 = E_{11} + E_{22} + E_{33} + 2(E_{44} + E_{55} + E_{66}) = \kappa\sigma^2 \quad [6]$$

$$\kappa = F_{11} + F_{22} + F_{33} + 2(F_{44} + F_{55} + F_{66})$$

$$= \mathrm{Tr}(\mathbf{F}) + F_{44} + F_{55} + F_{66}. \quad [7]$$

Because the errors in **C** are uncorrelated and have equal variance, we would expect that $\sigma_\mathbf{D}^2$ would not have any dependence on the DW gradient directions. That might be the case if **D** were calculated directly from **C**; in fact, **D** is calculated from the transformed version $\mathcal{A}\mathbf{C}$ of **C**, which is the solution of the linear system of Eq. [3]. Noise in the elements of $\mathcal{A}\mathbf{C}$ is neither uncorrelated nor of equal variance and depends on $\mathcal{A}$. The scalar dimensionless parameter κ depends only on the DW gradient directions employed by a DTI acquisition scheme and is the multiplying factor which transforms the equal variance of the uncorrelated errors in the elements of **C** to the total variance of the elements of the diffusion tensor **D**. Parameter κ provides a measure of the stability of the linear system of Eq. [4] in the presence of noise; equivalently, κ quantitatively estimates the independence of the 6D vectors **b** making up the $\mathcal{B}$ matrix. We therefore term the scalar κ the *index* of the DTI scheme.

Physical Meaning of the Index

Definition of the index κ from Eqs. [6] and [7] was based on the assumption that the covariance matrix of the errors in **C** is proportional to the unity matrix. We investigate now the physical implications of this assumption, in a validation of the practical use of the index κ.

The ith element C_i of **C** is $C_i = 1/B_i\ln(S_0/S_i)$. The error δC_i in C_i comes from the uncorrelated errors δS_0 and δS_i in S_0 and S_i, respectively, so that

$$\delta C_i = \frac{1}{B_i}\frac{1}{S_0}\,\delta S_0 - \frac{1}{B_i}\frac{1}{S_i}\,\delta S_i. \quad [8]$$

The covariance matrix of the errors in **C** becomes diagonal when the errors δC_i are uncorrelated (*23*) or, equivalently, when they are determined mainly by the error δS_i of the DW signal S_i and not by the error δS_0 of the common baseline signal S_0. According to Eq. [8], this condition is satisfied if $S_i \ll S_0$, so that the term containing δS_0 can be neglected. Because $S_i = S_0\exp(-B_i\mathrm{ADC}_i)$, where ADC_i is the apparent diffusion coefficient (ADC) (*21, 24, 25*) along the ith DW gradient direction, it follows that B_i should be sufficiently high in order to achieve the above strong inequality. Under that

condition, it is easy to show that the variance $\sigma_{C_i}^2$ of the element C_i is

$$\sigma_{C_i}^2 = \frac{\exp(2B_i\mathrm{ADC}_i)}{B_i^2\mathrm{SNR}_0^2},$$

where SNR_0 is the signal-to-noise ratio (SNR) of the common baseline signal S_0.

The resultant diagonal covariance matrix of the errors in **C** then becomes proportional to the unity matrix if all the $\sigma_{C_i}^2$ are equal. A general case which satisfies that condition is when the same b value B is used for all the DW acquisitions ($B_i = B$) and the scalar ADC is the same along all the applied DW gradient directions ($\mathrm{ADC}_i = \mathrm{ADC}$). The latter is the case of an isotropic medium (*2*). Thus, all the $\sigma_{C_i}^2$ have the same value σ^2,

$$\sigma^2 = \frac{\exp(2B\,\mathrm{ADC})}{B^2\mathrm{SNR}_0^2}. \quad [9]$$

The index is therefore proportional to the total variance of the elements of the measured diffusion tensor **D** of an isotropic medium, assuming that the DTI acquisition scheme employs the same, strong b value for each DW acquisition. Then, according to Eq. [6], the index can quantify absolutely the total variance of **D** if it is multiplied by the common variance of the elements of **C** given by Eq. [9]. Furthermore, as Eq. [6] implies, an experimentally measured value of κ can be derived from a DTI experiment on a isotropic medium, if the same strong b value is used for all the DW acquisitions: one then has to measure $\sigma_\mathbf{D}^2$ and divide the result by the σ^2 of Eq. [9].

Evaluation of the Noise Performance of a DTI Scheme

Since the index κ depends only on the DW gradient directions, it cannot discriminate between DW acquisitions performed using the same sets of DW gradient directions but with different gradient magnitudes and, therefore, different b values. Thus, the index treats all the DW acquisitions along the same DW gradient direction as equivalent, performing a form of signal averaging. For example, doubling the number of DW acquisitions per DW gradient direction will halve the value of the index. Generally, for a given number of DW gradient directions and acquisitions, the smaller the index value for a DTI scheme, the better its noise behavior.

Evaluation of a DTI scheme according to the presented theory requires comparison of the index value for the scheme to the optimum (minimum) index value for the N number of DW acquisitions employed by the DTI scheme. Calculation of that minimum considers the index as a function of the N free DW gradient directions, each of them being described by the pair of spherical coordinates (θ, ϕ); the value of the index κ is minimized relative to these pairs of angular variables via a multidimensional minimization routine (*22*).

Table 1 gives the values of this minimum for different

TABLE 1
Value of the Index κ for Various DTI Schemes[a]

DTI acq. scheme	Index value
A (6 DW acq.)	7.50
B (6 DW acq.)	12.00
C (7 DW acq.)	9.625
6	6.75
7	5.80
8	5.11
9	4.50
10	4.05
11	3.68
12	3.38

[a] Minimum value of the index κ for DTI schemes with different number of DW gradient directions with one DW acquisition each. The value of the index for the three conventional schemes A, B, and C with one DW acquisition per DW gradient direction is also shown.

numbers of DW gradient directions and acquisitions. It shows that the optimum value of the index κ varies inversely proportionally to the total number of DW acquisitions (and DW gradient directions). It also provides the value of the index for the three commonly used DTI acquisition schemes. These employ six gradient directions which are determined by six pairs of spherical angles (θ, ϕ), expressed in degrees.

For scheme A (*4, 9, 11*): (θ, ϕ) = (45°, 0°) (45°, 180°) (45°, 90°) (45°, 270°) (90°, 45°) (90°, 135°). Figures 1a and 1b provide visualization of the DW gradient directions for scheme A. For scheme B (*3, 8*): (θ, ϕ) = (90°, 0°) (90°, 90°) (0°, 0°) (90°, 45°) (45°, 0°) (45°, 90°). Figures 1c and 1d provide visualization of the DW gradient directions for scheme B. Scheme C (*1, 2, 18, 19, 26*) is a variant of scheme B, and employs a seventh DW gradient direction: (θ, ϕ) = (54.74°, 45°). The indices for these three conventional schemes were calculated considering one DW acquisition per DW gradient direction. In addition to the DW acquisitions, the schemes all involve one additional baseline acquisition without diffusion-weighting.

Schemes A and B have significantly different index values: the index value of scheme A is 1.11 times the optimum value for six DW acquisitions, while that of scheme B is 1.78 times the same optimum value. As a result, scheme A would be expected to show better noise performance than scheme B, given that for both schemes the same number of DW acquisitions per DW gradient direction are performed using the same b values. In addition, the index κ for scheme A is only 1.11 times the corresponding minimum; therefore, for DTI schemes employing six DW gradient directions, scheme A is almost optimum. Adding one DW gradient direction to scheme B leads to scheme C, which has an index value of 9.625 or 1.66 times the corresponding optimum index value for seven DW acquisitions. Although the index value for scheme C is slightly improved when compared to that of scheme B, it is still significantly worse than that of scheme A, even though scheme C employs one more DW gradient direction than schemes A and B. Therefore, the present analysis will consider only the two con-

ventional schemes A and B employing the same-multiple-of-six number of DW acquisitions, omitting scheme C.

Development of New DTI Acquisition Schemes

The presented theory provides also a novel method for the development of new DTI acquisition schemes. This study has considered a scheme which employs N different DW gradient directions with one DW acquisition each together with one baseline acquisition without diffusion-weighting. In order to be directly comparable to the conventional schemes A and B, the new schemes should employ multiple of 6 total number N of DW acquisitions. We have therefore considered the case for $N = 12$; this corresponds to 2 DW acquisitions per DW gradient direction for schemes A and B.

The DW gradient directions of the new scheme were derived from minimization of the value of the index κ, for 12 independent DW gradient directions. Although the minimum value of the index was unique (see Table 1), the set of the DW directions which yielded that minimum was not unique because the index is rotationally invariant (its value remains the same when the directions it examines are rotated as a whole), and also, the total number of DW directions (*12*) exceeds the dimension (*6*) of the space of **b** vectors. Furthermore, the optimum value of the index κ could also be achieved by employing only 6 discrete DW directions (those which optimized the value of the index for 6 independent DW directions) with 2 DW acquisitions at each one of them. Nevertheless, such a scheme was not considered because it is essentially a mere variation of the two commonly used 6-DW-direction schemes: all of those schemes sample the 6D space of the **b** vectors in only 6 discrete directions.

We have called the proposed scheme scheme 12, as it employs 12 DW gradient directions and acquisitions. The pairs of the spherical angles (θ, ϕ) which define these DW gradient directions are (θ, ϕ) = (53°, 19°) (20°, 274°) (61°, 76°) (59°, 124°) (48°, 238°) (42°, 157°) (68°, 307°) (73°, 184°) (72°, 335°) (18°, 42°) (88°, 218°) (82°, 268°). Figures 1e and 1f provide visualization of the DW gradient directions for scheme 12.

METHODS

Simulations

Simulations were applied to the two conventional schemes A and B and the proposed scheme 12, all of them employing 12 DW acquisitions. These used four types of cerebral fibers that all had the same mean diffusivity D_m (mean value of the trace of **D**) of 0.7×10^{-3} mm^2/s, close to experimental findings for the mean diffusivity for healthy cerebral matter (*9, 18*). The smallest principal diffusivity for the anisotropic fiber types was 0.15×10^{-3} mm^2/s, very close to the smallest calculated principal cerebral diffusivity (*9*). Similarly, the highest diffusivity in the simulations, which corresponded to the highest diffusivity for the cylindrical fiber, approximated the largest calculated principal cerebral diffusivity in (*9*). The four types of fibers were
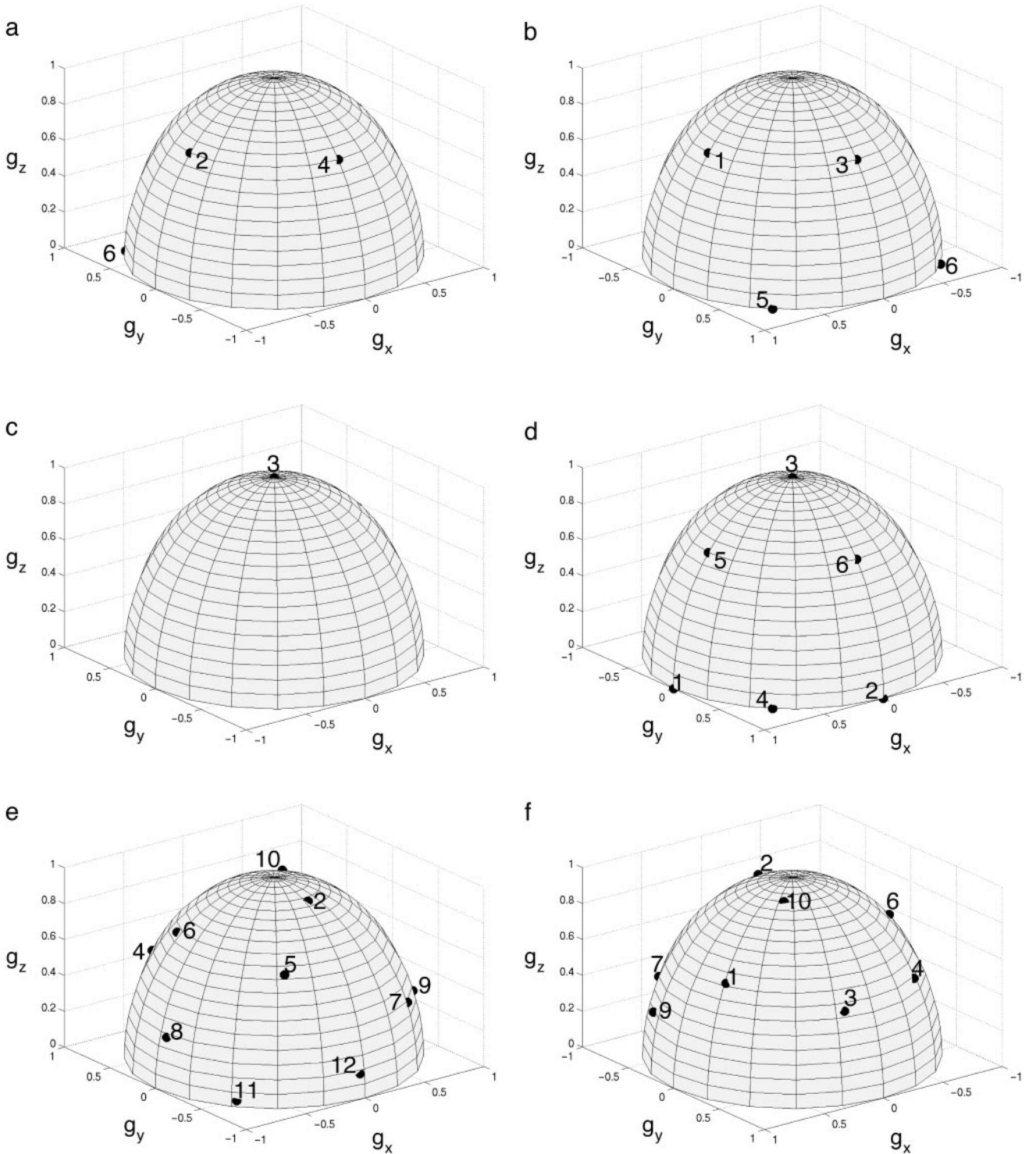
FIG. 1. Visualization of the DW gradient directions of the three DTI acquisition schemes A, B, and 12. The position of the tip of the unity vectors g_i for each scheme is shown on the surface of the unity radius semisphere. Because of the equivalence of the $\pm g_i$ for DTI, all g_i have $g_{zi} \geq 0$. Two views, front and rear, are shown, having an azimuthial angular difference on the g_x, g_y plane of 180°; hence, the different orientation of the g_x, g_y axes. For each DTI scheme, numbering of the directions corresponds to the order these are defined in under Theory. (a) and (b) Front and rear views for scheme A. (c) and (d) Front and rear views for scheme B. (e) and (f) Front and rear views for scheme 12.

(a) cylindrical fibers with diffusivities 1.8×10^{-3} mm^2/s, 0.15×10^{-3} mm^2/s, and 0.15×10^{-3} mm^2/s,

(b) disc-shaped fibers with diffusivities 0.975×10^{-3} mm^2/s, 0.975×10^{-3} mm^2/s, and 0.15×10^{-3} mm^2/s,

(c) isotropic fibers with three equal diffusivities 0.7×10^{-3} mm^2/s, and,

(d) generally anisotropic fibers with diffusivities 1.25×10^{-3} mm^2/s, 0.7×10^{-3} mm^2/s, and 0.15×10^{-3} mm^2/s.

The b value B used in scheme 12 was chosen to correspond to the maximum sensitivity of a 2-point ADC measurement (27), i.e., $B = 1.1/(0.7 \times 10^{-3} \text{ mm}^2/\text{s}) \simeq 1570 \text{ s/mm}^2$, when applied to an isotropic fiber with diffusivity equal to the mean diffusivity D_m. Realization of schemes A and B, with two DW acquisitions per DW gradient direction, used b values $B = 1570 \text{ s/mm}^2$ and $B_1 = B/2 = 785 \text{ s/mm}^2$. In addition, those two conventional schemes were applied using the same b value B for both the DW acquisitions per DW gradient direction.

Each fiber type was aligned with the DW gradient frame of reference to give a diagonal matrix **D**. The "ideal" DW signal was calculated from Eq. [1], assuming a constant ideal value of the baseline signal $S_0 = 100$, for each fiber type and DTI scheme. Complex Gaussian noise was then superimposed upon the ideal signals to provide the complex noise-contaminated signals and their magnitude was then obtained. The noise values were generated using the routine *gasdev* (22) and scaled so that the SNR_0, defined as (ideal S_0)/(standard deviation of noise), could be set to any desired level. The six independent elements of **D** and the ideal baseline signal S_0 were fitted simultaneously to all the generated signals from each scheme using a nonlinear least-squares fitting routine (22) to the sets of equations of the form of Eq. [1]. We did not apply the standard linear least-squares curve-fit to the logarithm of the signals to avoid additional errors from the logarithmic scaling of noise at low SNR_0 values (8). Having calculated the six independent elements of **D**, the square of the error for each of these elements was calculated by subtracting the fitted values from the ideal diffusion tensor elements. For each fiber type, DTI acquisition scheme, and SNR_0 value, the above procedure, noise generation → creation of noisy data → fitting → error calculations, was repeated 8192 times and the variance of the error for each of the diffusion tensor elements was calculated as the mean value of the square of the corresponding error. Therefore, the total variance of the measured diffusion tensor was calculated for each type of fiber, DTI acquisition scheme, and SNR level of the baseline signal.

Experiments

DTI experiments were performed in a cylindrical phantom of distilled water (18 cm internal diameter (id)) and the brain of a healthy volunteer, using schemes A, B, and 12, all of them employing 12 DW acquisitions.

The experiments were performed at 2 T in an horizontal-bore, 100-cm-id, superconducting magnet (Oxford Magnet Technology, Oxford, UK) attached to a Bruker MSL 400 console, running Tomikon imaging software (version 890601, Bruker Medizin Technik GmBH., Karlsruhe, Germany). The gradient set was a homebuilt, unshielded set (id = 35 cm) designed by a genetic algorithm (28); each coil of the gradient set was driven by a pair of Techron amplifiers (Model 7770, Crown International Inc., Elkhart, IN). The radiofrequency (RF) head coil used was a purpose-built (id = 25 cm), 8-strut quadrature "birdcage" design (29).

DW interleaved echo-planar imaging (DW-IEPI) (30, 31) was implemented by inserting a pair of Stejskal–Tanner rectangular gradient pulses (20) in a homebuilt spin-echo echo-planar sequence. The duration δ of the DW gradient pulses was 28 ms and their temporal spacing Δ was 66 ms.

For the phantom experiment, scheme 12 employed the b value $B = 486 \text{ s/mm}^2$, which corresponded to optimum noise performance for a 2-point ADC measurement, as described under Simulations, assuming an ADC value of water $2.26 \times 10^{-3} \text{ mm}^2/\text{s}$ at 25°C (32) ($486 \text{ s/mm}^2 = 1.1/(2.26 \times 10^{-3} \text{ mm}^2/\text{s})$). Schemes A and B were implemented using two different b values $B = 486 \text{ s/mm}^2$ and $B_1 = B/2 = 243 \text{ s/mm}^2$ per DW gradient direction. In addition, the schemes A and B were applied using the same b value $B = 486 \text{ s/mm}^2$ for both the DW acquisitions per DW gradient direction. For the *in vivo* experiment, scheme 12 applied the b value $B = 1570 \text{ s/mm}^2$ while schemes A and B applied the b values $B = 1570 \text{ s/mm}^2$ and $B_1 = B/2 = 785 \text{ s/mm}^2$ per DW gradient direction. The *in vivo* implementation of schemes A and B using the pair (B_1, B), rather than the pair (B, B) of b values per DW gradient direction, is justified in the subsection "Multiple acquisitions per DW gradient direction: The choice of b values" under Results.

Single-slice (for the phantom) and multislice (four contiguous slices, for the human brain) transverse images with field of view of 25 cm and slice thickness of 5 mm (for the phantom) and 7 mm (for the human brain) were acquired. Four interleaves were acquired for each image. This yielded a 128×128 acquisition matrix, which provided a 256×256 image, after symmetric zero-padding in both directions and Fourier transformations. Imaging with partial (62.5%) k-space coverage was performed (31, 33). For the *in vivo* experiments, ECG-gated acquisitions (34, 35) and the use of a navigator echo (36–38) in the read direction were used in order to minimize motion artifacts between the interleaves. For the phantom experiment the navigator echo was kept in the pulse sequence, so that both the phantom and the *in vivo* experiments had an identical sequence of imaging gradients. Echo time (TE) was 118 ms and the repetition time (TR) was set to 4 RR intervals ($\simeq$4.4 s) for the *in vivo* experiment, acquiring data from one slice per RR interval, and to 2 s for the phantom experiment. Two "dummy" scans were performed in both the experiments in order to sufficiently bring the signal from the long T_1 components (cerebrospinal fluid (CSF) for the *in vivo* experiment and water for the phantom experiment) to the steady state, thus avoiding ghosting artifacts. The total acquisition time for the entire dataset of each DTI scheme was therefore 2.6 min for the phantom experiment and about 5.7 min for the *in vivo* experiment. The sequence of the imaging gradients had been designed so that they were rephased as soon as possible after their application, so that their contribution to **b** and $\mathcal{B}$ could be considered negligible (19, 26), as discussed above. Prior to DW-IEPI acquisitions, automated shimming (39) was performed in both the phantom and the brain in order to ensure optimised static field homogeneity over the regions of interest.
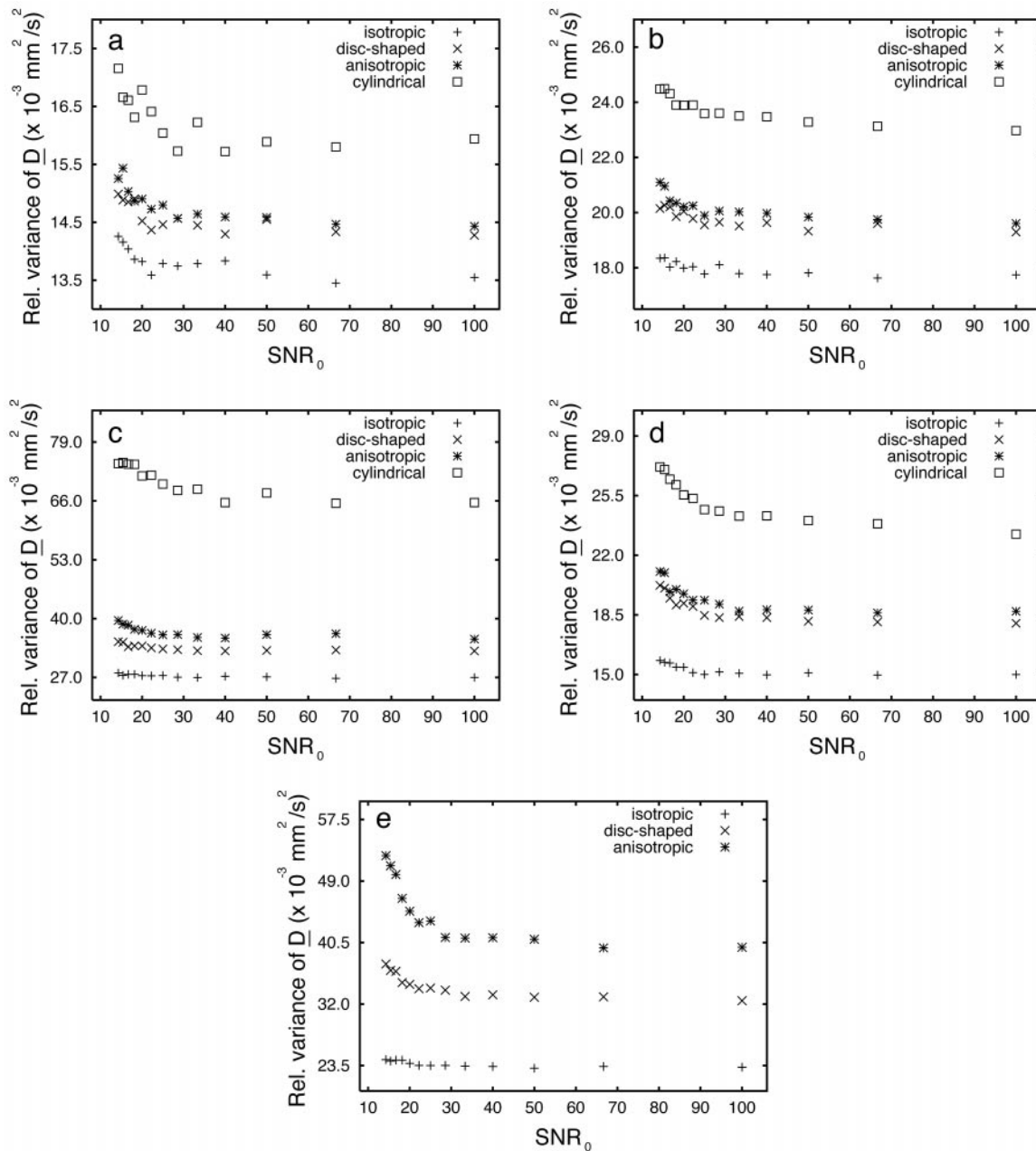
FIG. 2. Total variance of **D**, normalized by multiplication by the square of the SNR of S_0, for various SNR values of S_0 and for each of the four fiber types. The compared DTI schemes employed 12 DW acquisitions. (a) Results from the proposed scheme 12 using the b value B for all the DW acquisitions. (b) and (c) Results from the conventional schemes A and B, respectively, using the pair $(B/2, B)$ of b values per DW gradient direction. (d) and (e) Results from the conventional schemes A and B respectively using the pair (B, B) of b values per DW gradient direction. Note the different scaling of the variance for each plot.

The DW-IEPI data for each experiment were fitted using the same processing routines as for the simulations and the six elements of the diffusion tensor **D** were calculated pixelwise. For the phantom data, a central homogeneous region comprising 8000 pixels was selected and the mean and the variance of the diffusion tensor elements and the total variance of the diffusion tensor were calculated. For the human brain data, maps of the rotationally invariant isotropy index (mean value of the trace Tr(**D**) of **D**) and the

rotationally invariant index volume ratio (1-VR)) (*8, 9, 18*) were calculated.

RESULTS

Simulations

Figure 2 shows the results from the simulations. It plots the total variance of the measured **D** normalized by SNR_0 (i.e., the

absolute variance of **D** has been multiplied by the square of SNR_0), for various SNR_0, for each fiber type, and for each DTI scheme (scheme 12, scheme A, and scheme B). The normalization made the plotted results independent of SNR_0 (cf., Eqs. [6] and [9]). As described earlier, we have considered two implementations of the schemes A and B. In the first, two DW acquisitions per DW gradient direction were performed at different b values (Figs. 2b and 2c); in the second, these acquisitions were performed at the same b value (Figs. 2d and 2e). Note that the scaling of the relative variances for the plots in Fig. 2 is different, and that for scheme B, using the same b value for all the DW acquisitions (Fig. 2e) gives a very high relative variance for the cylindrical fiber, which exceeds the range of values displayed in Fig. 2e.

Validation of the index. Under Theory the index κ was developed, which is proportional to the total variance of **D** for an isotropic medium, when all the DW acquisitions were obtained under the same high b value. Table 1 indicates that the ratio between the index value for scheme A with 12 DW acquisitions and that for scheme 12 is $(7.50/2)/3.38 \simeq 1.11$, whereas the ratio between the index value for scheme B with 12 DW acquisitions and that for scheme 12 is $(12.00/2)/3.38 \simeq 1.78$. Figures 2a, 2d, and 2e demonstrate a calculated ratio between the variance of **D** for schemes A and 12 of about $15.0/13.5 \simeq 1.1$ that remains well-bounded at that value, for the case of the isotropic fiber. It also demonstrates a calculated ratio between the variance of **D** for schemes B and 12 of about $23.5/13.5 \simeq 1.74$ that also remains well-bounded at that value. These results closely agree with the theoretical predictions. Furthermore, under Theory the condition $S_i \ll S_0$ was adopted, where S_i are the DW signals and S_0 is the common baseline signal, in order to ensure that the errors in **C** were uncorrelated. Yet, this condition did not hold for the simulations: for the isotropic fiber it was $S_i = S_0\exp(-1.1) \simeq 0.33S_0$. Therefore, the empirical findings demonstrate that the condition $S_i \ll S_0$, or equivalently the requirement for high b value, can be relaxed, without compromising the validity of our analysis.

Multiple acquisitions per DW gradient direction: The choice of b values. Because the b value B corresponded to the optimum 2-point ADC calculation for the isotropic case, we expect that the error in the calculation of **D** for the isotropic case will be smaller for the implementation of schemes A and B using twice the b value B per DW gradient direction than for the implementation of the respective schemes using b values $B/2$ and B per DW gradient direction. As a result, the variance σ_D^2 for the isotropic case is smaller in Figs. 2b and 2c than in Figs. 2d and 2e, respectively. On the other hand, the anisotropic fibers examined had principal diffusivities on either side of the isotropic diffusivity, and we cannot predict analytically which pair of b values (($B/2$, B) or (B, B)) per DW gradient direction will have the best noise performance for schemes A and B. However, the simulations show that applying schemes A and B, using (B, B) tends to lead to increased σ_D^2, especially for cases of low SNR_0 (<30) and for strongly anisotropic fibers
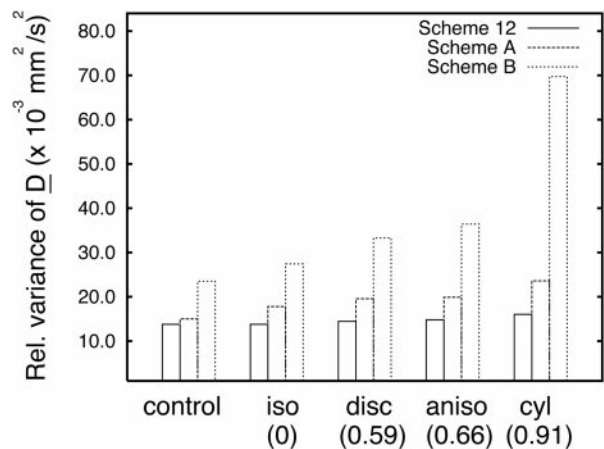

FIG. 3. Dependence of noise sensitivity of the DTI schemes on fiber anisotropy. For scheme 12, using the b value B for all the DW acquisitions, and for schemes A and B, using the pair ($B/2$, B) of b values per DW gradient direction, the total normalized variance of **D** (Figs. 2a–2c, $SNR_0 = 25$) is plotted for the four fiber types, classified according to their anisotropy index $1 - VR$, which is shown in parentheses. Additionally, the respective total normalised variance of **D** corresponding to the index κ (Figs. 2a, 2d, and 2e, $SNR_0 = 25$) is shown under the label "control."

(cylindrical fiber). Therefore, for the rest of the analysis, we have considered the implementation of schemes A and B using the pair ($B/2$, B) of b values per DW gradient direction.

Evaluation of the performance of DTI schemes for anisotropic fibers. The implementation of schemes A and B using the pair ($B/2$, B) of b values per DW gradient direction renders the presented theoretical analysis of error propagation not applicable. However, for such cases, the total variance of **D** can be compared with the measurable quantity which corresponds to the physical meaning of the index κ (i.e., the total variance of **D** of an isotropic medium with mean diffusivity equal to the mean diffusivity of the anisotropic case, measured with the same b value for all the DW acquisitions). Such comparison was facilitated by monitoring the results of the simulations of Figs. 2a–2c for a given value of SNR_0. Figure 3 gives the results for $SNR_0 = 25$ together with the total variance of **D**, which physically corresponds to the index κ (derived from Figs. 1a, 1d, and 1e, for schemes 12, A, and B, respectively, and for $SNR_0 = 25$). Therefore, Fig. 3 enables evaluation of noise propagation for schemes 12, A, and B in two ways.

(a) Comparisons between schemes: for each individual fiber type, the relative variance of **D** was smallest for scheme 12 and largest for scheme B. Furthermore, for each type of fiber, the ratio of the variance between two schemes, for example, the ratio between the variance for scheme A and scheme 12 or the ratio between the variance for scheme B and scheme 12, never became smaller than the ratio of the variance corresponding to the index of the respective schemes.

(b) Comparisons within schemes: the total variance of **D** within each scheme was smallest for the isotropic fiber and largest for the most anisotropic, cylindrical fiber. Additionally,

TABLE 2
Mean Values of the Elements of D of the Isotropic Phantom[a]

Mean value (×10⁻³ mm²/s)	Scheme 12	1 b value		2 b values	
		Scheme A	Scheme B	Scheme A	Scheme B
D_{xx}	2.295	2.263	2.243	2.247	2.293
D_{yy}	2.242	2.291	2.287	2.271	2.252
D_{zz}	2.274	2.238	2.275	2.279	2.284
D_{xy}	0.024	0.035	0.036	0.010	0.041
D_{xz}	0.036	0.038	0.049	0.044	0.034
D_{yz}	−0.039	−0.046	−0.011	−0.028	−0.037

[a] Mean values of the six independent elements of **D** for the isotropic phantom using different DTI acquisition schemes calculated over the selected ROI, which consisted of 8000 pixels.

for either scheme A or B, the variance in **D** for each fiber exceeded the "control" variance corresponding to the index of the respective scheme.

The total variance of **D** thus depended on the shape of the effective diffusion ellipsoid corresponding to the fiber. This dependence was weakest for scheme 12, in which the variance for the cylindrical fiber was about $16.0/13.5 \simeq 1.19$ times the variance for the isotropic fiber. It was the strongest for scheme B, in which the variance for the cylindrical fiber was about $70.0/27.0 \simeq 2.59$ times the variance for the isotropic fiber. Note also that for scheme A, which has an index value close to the optimum value of scheme 12, the variance also changed a little between the types of fibers. Thus, in this case, the variance for the cylindrical fiber was about $24.0/18.0 \simeq 1.33$ times the variance for the isotropic fiber.

Therefore, for any DTI scheme irrespective of whether it employs the same or different b values for all the DW acquisitions per DW gradient direction, the relative variance of **D** for anisotropic fibers is always higher than that for the isotropic fibers, when the latter is measured using a single b value for all the DW acquisitions. Since the variance of **D** for the isotropic case, using the same b value for all the DW acquisitions per DW gradient direction is associated with the index κ of the

scheme, the index provides a lower limit on the noise propagation for a DTI scheme: the relative variance of **D** will depend on the diffusion "shape" of the fiber considered and on the b values used by the DTI scheme, but it will never be less than the relative index of the scheme. In addition, the smaller the value of the index for a DTI scheme, or equivalently, the closer to the optimum its index value, the weaker the dependence of noise propagation on the various levels of the fiber diffusion anisotropy.

Phantom Study

Tables 2 and 3 summarize the results from the statistical analysis of the measured **D** over the selected region of interest (8000 pixels) of the water phantom for the examined DTI schemes. Table 2 gives the mean values of the six independent elements of **D**, while Table 3 gives their variance and the total variance of **D**. For each scheme the mean values of the diagonal element of **D** varied by less than 2% from the reported value of the diffusion coefficient D_0 of pure water at the temperature of the measurements ($D_0 = 2.26 \times 10^{-3}$ mm²/s at 25°C) (32). Similarly, the magnitude of the mean values of the off-diagonal elements of **D** was kept very small, being less than 3% of D_0. Obviously, for each scheme, the measured **D**

TABLE 3
Variance of the Elements of D of the Isotropic Phantom[a]

Variance (×10⁻⁴ mm²/s)²	Scheme 12	1 b value		2 b values	
		Scheme A	Scheme B	Scheme A	Scheme B
D_{xx}	0.17	0.24	0.18	0.27	0.19
D_{yy}	0.15	0.25	0.16	0.28	0.19
D_{zz}	0.16	0.22	0.19	0.26	0.17
D_{xy}	0.08	0.05	0.19	0.10	0.21
D_{xz}	0.08	0.07	0.21	0.07	0.20
D_{yz}	0.06	0.07	0.17	0.08	0.21
D	0.92	1.09	1.67	1.31	1.79

[a] Variances of the elements of **D** and total variance of **D** for the isotropic phantom using different DTI acquisition schemes, calculated over the selected ROI, which consisted of 8000 pixels.
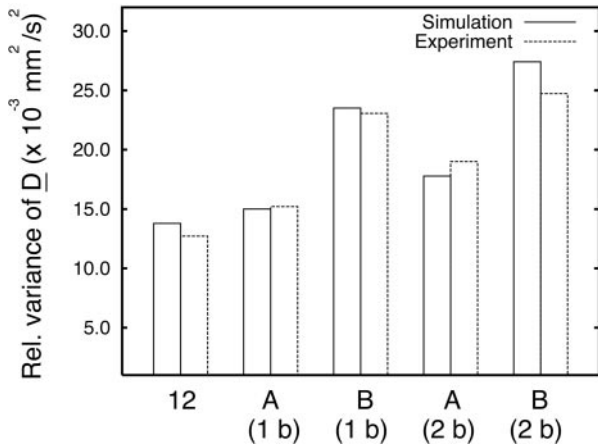
FIG. 4. Comparison of the total normalized variance of **D** from the experiments on the isotropic phantom (Table 3) with that from the simulations (Fig. 2, isotropic case, $SNR_0 = 25$). Implementation of schemes A and B using the pair of b values (B, B) and $(B/2, B)$ is denoted as 1b and 2b, respectively. As explained in the text, the results from the experiments have been scaled appropriately in order to correspond to the same b values and isotropic diffusivity as those used in the simulations.

has the structure of a diagonal tensor, proportional to the 3×3 unity tensor, corresponding to an isotropic medium. Therefore, the calculations of the $\mathcal{B}$ matrix for each scheme, considering only the DW gradients and not the imaging gradients, were valid.

The variances of the elements of **D** (Table 3) correspond to standard deviations which are smaller than 3% of D_0. In common with the simulations, the phantom study showed that for schemes A and B, the total variance of **D** was higher when different b values were used for the DW acquisitions performed at the same DW gradient direction than when a single b value was used.

The measured absolute total variances of **D** in Table 3 can be compared with the respective normalized variances of **D** in Table 3 can be compared with the respective normalized variances of **D** for the isotropic fiber in the simulations (Fig. 2). Such comparison requires appropriate scaling of the absolute values of σ_D^2 listed in Table 3, so that they correspond to the same isotropic diffusion coefficient and b values as the ones employed in the simulations. For schemes using a single b value, and for both the simulations and the experiments, that b value was selected such that $B \cdot ADC \simeq 1.1$. It follows from Eqs. [6] and [9] that each of the σ_D^2 of Table 3 was scaled (multiplied) by the factor $(SNR_1 \cdot B_1/B_2)^2$, where SNR_1 is the SNR_0 for the phantom experiments (equal to 120), and B_1 and B_2 are the b values for the phantom experiments and the simulations, respectively. Scaling for the implementations of schemes A and B used as a unique b value the highest of those two used in each implementation. According to Methods, that b value was still given by $B \cdot ADC \simeq 1.1$, both for the simulations and for the phantom experiments. Figure 4 compares the scaled experimental σ_D^2 with the respective σ_D^2 from the simulations of the isotropic case (the normalized value σ_D^2

of the simulated results was taken from the point $SNR_0 = 25$ in Fig. 2 for the isotropic case). The very good agreement of the results from the experiments on the isotropic phantom with the results of the simulations (Fig. 4) not only confirms the correspondence of the index κ to the total variance of **D** for an isotropic medium, when the DTI scheme uses the same b value for all the DW acquisitions. It also verifies the difference in noise propagation between the two conventional schemes A and B. Furthermore these results show that the proposed scheme 12 has better noise performance than either of those two schemes, as predicted by both the theory of the index and the simulations.

Determination of the Index κ from DTI Measurements

The results from the simulations and from the phantom experiments were also used for practical determination of κ according to Eqs. [6] and [9]. Therefore, we considered the implementation of schemes A and B using the pair (B, B) of b values per DW gradient direction. For the simulations, the values of σ_D^2 were taken from Figs. 2a, 2d, and 2e, for $SNR_0 = 25$ for the isotropic case. Figure 5 plots that calculated κ for each DTI scheme, as it was derived from the simulations and the phantom experiments, together with the respective theoretical values of κ, from Table 1.

The very good agreement between the theoretical and the measured values of the index κ for each scheme verifies the validity of the direct calculation of κ from experimentally measurable quantities. Therefore, the consistency of the theoretical analysis has been successfully demonstrated not only through relative comparisons of the noise performance of the DTI schemes for various cases of fiber anisotropy (Figs. 2, 3, and 4), but also through the direct calculation of the index κ from measured quantities (Fig. 5).
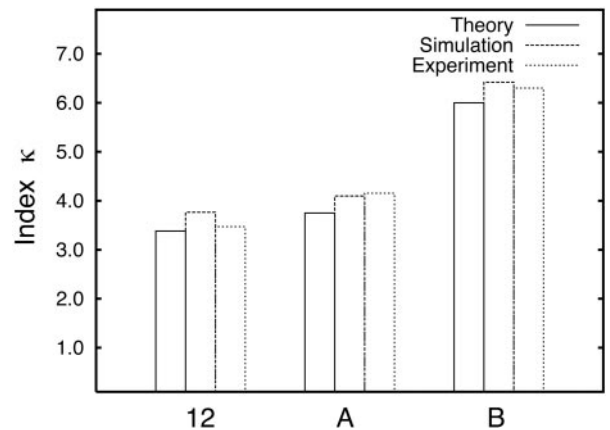

FIG. 5. Measured value of the index κ (Eqs. [6] and [9]) for each DTI scheme (12, A, and B), using the results from the simulations (Figs. 2a, 2d, and 2e, isotropic case, $SNR_0 = 25$) and from the experiments on the isotropic phantom (Table 3). Additionally, the theoretical value of κ (Table 1) is shown for each scheme.
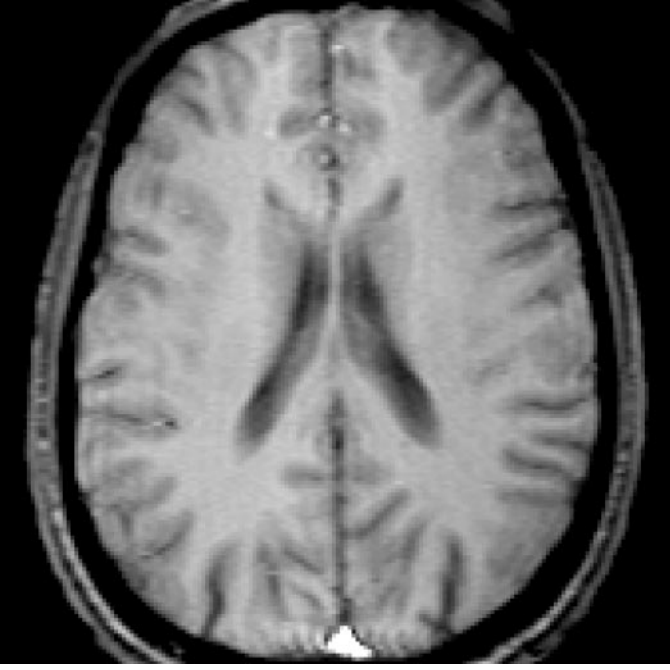
FIG. 6. Anatomical T_1-weighted image of one transverse slice selected for the DTI experiments. Repetition time: 200 ms, echo time: 8.5 ms, and image matrix: 256×256.

DTI Experiments in the Human Brain

Figure 6 shows the anatomical T_1-weighted image of one representative slice selected for the DTI experiments. Figures 7 and 8 show the calculated maps of the mean value of the trace of **D** (mean diffusivity), and those of the anisotropy index 1-VR, for each examined DTI scheme (scheme 12, scheme A, and scheme B; the last two using two DW acquisitions with different b values per DW gradient direction). The mean diffusivity maps (Fig. 7) have been scaled from 0 to 1.5×10^{-3} mm^2/s, while the anisotropy maps (Fig. 8) have been scaled from 0 to 1.

Mean diffusivity maps. The mean diffusivity maps (Fig. 7) showed excellent uniformity over the cerebral matter (gray and white), for every scheme examined. This uniformity reflects nearly constant mean diffusivity ($\simeq 0.7 \times 10^{-3}$ mm^2/s), as has been reported for healthy cerebral matter (*8, 9, 18*).

This uniformity of the mean diffusivity maps was particularly evident in the cortical regions, which are composed of almost isotropic gray matter. The intermingling gray and white matter in deeper cerebral areas which could result in various degrees of anisotropy caused small variations of the mean diffusivity in the form of hypointense regions in the mean diffusivity maps. Such regions appeared smaller and smoother for the case of the proposed scheme 12; schemes A and B gave maps with very similar nonuniformities.

In general, there were relatively small differences in mean diffusivity maps obtained by the three compared DTI schemes. This reflects the calculation of the mean diffusivity, which does not use the full information from the six independent elements of **D**, but rather considers only its three diagonal elements. The noise in the mean diffusivity for each scheme consequently depends not only on the overall noise performance of the DTI scheme as represented by the index κ and the results from the simulations, but also on the relative distribution of noise between the diagonal and off-diagonal elements of **D**. For example, according to their index values (Table 1), scheme A has better noise behavior than scheme B; however, the results of the phantom study (Table 3) show that the variance of the diagonal elements for scheme A is higher than that for scheme B, in an isotropic medium. These two effects tend to balance out, leading to very similar qualities in the maps of the mean diffusivity between schemes A and B. On the other hand, for scheme 12, which has the best noise performance for total **D** (Fig. 2), the variance of the diagonal elements is smaller than that of the other two schemes for an isotropic medium (Table 3); these two effects cause the mean diffusivity maps to appear slightly smoother and more uniform than those derived by schemes A and B.

Treatment of CSF. The mean diffusivity maps obtained using scheme 12 showed some CSF-filled areas with a lower intensity than did the two other schemes. Such areas included the ventricular regions, the anterior horns of the lateral ventricles, and various sulci, and they may also contain contributions from the surrounding gray matter. The mean value of the mean diffusivity over those areas was 2.745×10^{-3} mm^2/s for scheme 12, 3.214×10^{-3} mm^2/s for scheme A, and 3.172×10^{-3} mm^2/s for scheme B. The reduced value of the mean diffusivity for scheme 12 is because scheme 12 effectively employed 2-point ADC measurements, one baseline signal acquisition at $b = 0$ and one DW acquisition at $b = 1570$ s/mm^2, whereas both the conventional schemes A and B effectively employed 3-point ADC measurements with one baseline signal acquisition at $b = 0$ and two DW acquisitions at $b = 785$ and 1570 s/mm^2, respectively. It can be shown that the 2-point ADC calculation tends to give lower ADC values than the 3-point ADC calculation for signal containing contributions from both CSF and gray matter. The exact difference would be dependent on the relative contributions to the signal from CSF and gray matter. Furthermore, referring to the terminology in (*27*), while the b value used for scheme 12 covers cerebral diffusivities between 0.15 and 1.8×10^{-3} mm^2/s, with the DW sensitivity never less than 44% of the maximum, the corresponding DW sensitivity for CSF is about 9.5% of the maximum (assuming a CSF diffusion coefficient $\simeq 3.2 \times 10^{-3}$ mm^2/s (*9*)). In contrast, schemes A and B use the additional b value, 785 s/mm^2, and the respective DW sensitivity for CSF is about 58% of the maximum; this leads to more precise CSF measurements. However, cerebral DTI is primarily concerned with the cerebral matter rather than CSF.

FIG. 7. Mean diffusivity maps of the slice of Fig. 6 calculated by the three compared DTI schemes.

Anisotropy Maps

The anisotropy maps (Fig. 8) for each scheme distinguish the main strongly anisotropic cerebral structures (genu and splenium of the corpus callosum, forceps frontalis and occipitalis, centrum semiovale, optic radiations, and various white matter radiations towards the cortex) from those showing low anisotropy (cortical gray matter and caudate nucleus).

Although some differences in the maps can be attributed to slightly different slice positions used during application of the three schemes (as is the case for some variations in the appearance of the thin and short white matter radiations projecting from the cortex), the maps from the three schemes show significant differences in the appearance of noise, which reflect the different noise performance of the three compared schemes.

Between the two schemes A and B, scheme B yielded generally noisier anisotropy maps. Most of the anisotropic structures (for example, parts of the centrum semiovale on both hemispheres and many thin white matter radiations) suffered a grainy appearance with strong and discontinuous intensity variations. Furthermore the 1-VR map of scheme B delineated many white matter radiations poorly at coarse resolution or gave a blurred and diffuse representation of structures, such as the splenium of the corpus callosum. Other adverse features of the map of scheme B included the presence of high-intensity pixels close to the interface between low- and high-anisotropy structures (for example, the interface between the splenium of the corpus callosum and the lateral ventricles). For many high-intensity pixels which caused discontinuous appearance, the signal intensity exceeded the theoretical maximum unity value of 1-VR. That is the result of poor estimation of **D**: the smallest principal diffusivity for those pixels was negative. In contrast, scheme A yielded maps of significantly better quality that showed considerably less evidence of the noise-induced resolution problems described above. Most of the anisotropic structures were clearly defined and the intensities within many individual structures stayed reasonably uniform and smooth. However, some high anisotropy structures in the maps of scheme A showed still a noisy and grainy appearance (for instance, regions within the centrum semiovale). Finally, scheme 12 gave the smoothest anisotropy map having the most uniform intensity distribution within anisotropic structures.

Therefore, the anisotropy maps of the two conventional schemes A and B exhibited differences in noise performance, in qualitative agreement with the differences in the respective index values of the schemes. However, the index value for scheme A was very close to the optimum index value, and so the maps from schemes A and 12 could have a very similar quality with respect to noise appearance. This might be the case, if scheme A was compared with a scheme which optimized the index value using the same number of

DW gradient directions (6) as scheme A. However, scheme 12 employs 12 DW gradient directions, sampling the space of the effective diffusion ellipsoid more densely and more uniformly than scheme A. This is the main qualitative difference between the schemes A and 12, and, in fact, the cause of the differences between the maps of the two schemes.

DISCUSSION AND CONCLUSIONS

This study investigated the effect of the DW gradient directions of a DTI scheme on the noise in the measured diffusion tensor $\mathbf{D}$. In the absence of significant contributions from the imaging gradients, the DW gradient directions effectively determine the distribution of the scalar b value B between the elements of $\mathbf{D}$, or equivalently, the factors which weight the contribution of the elements of $\mathbf{D}$ in the argument of the exponential term describing the DW-induced signal attenuation (Eq. [1]). Treating the determination of $\mathbf{D}$ as a linear system of equations (Eq. [4]), we introduced the quantitative index κ, which evaluates the noise behavior of the linear system by examining the stability of the characteristic matrix $\mathcal{B}$ of this linear system. The index is rotationally invariant, depending only on the DW gradient directions, and it physically corresponds to the total variance of the measured $\mathbf{D}$ for an isotropic medium, using the same b value for all the DW acquisitions. Other quantities can also evaluate the stability of Eq. [4] in noise: they include the ratio between the maximum and minimum elements of the diagonal matrix $\mathbf{W}$, following SVD of the $\mathcal{B}$ matrix (22) and the total variance of the six independent elements of $\mathbf{D}$. However, such measures either lack the correspondence to physically measured quantities or are rotationally variant. The index κ provided an objective assessment of the noise performance of a DTI scheme: it is calculated and then compared with the minimum index value which can be achieved with the same total number of DW acquisitions.

A second novel contribution of this work is that it compared the noise performance of the two widely used DTI acquisition schemes (scheme A and scheme B), which in the published DTI literature have been used indiscriminately, because both of them employ six noncollinear DW gradient directions. Their index values are significantly different: for scheme A it is 1.1 times the minimum, while for scheme B it is 1.78 times the minimum. Based on this information one would expect scheme A to yield less noisy and more accurate measurements of $\mathbf{D}$ than scheme B.

A third novel aspect of this study is the use of the index as a means to develop new DTI schemes. For a given number N ($N \geq 6$) of DW gradient directions with one DW acquisition each, the DW directions of the scheme are chosen to minimize the value of the index. These schemes are different in concept from those currently used, because they use the redundant $N - 6$ DW acquisitions in order to

FIG. 8. Volume ratio (1-VR) maps of the slice of Fig. 6 calculated by the three compared DTI schemes.

sample the space of the effective diffusion ellipsoid more densely. In addition, the use of a single DW acquisition per DW gradient direction is validated because the mean diffusivity in gray and white matter of healthy human brain varies little between each other. Accordingly, the single b value B for each DW acquisition can be calculated as the one which gives the optimum performance for a 2-point (one baseline and one DW) measurement of that mean diffusivity, i.e., $B \simeq 1.1/\langle D \rangle$, where $\langle D \rangle$ is the mean diffusivity. As shown in (27), although that optimum b value corresponds exactly to a single ADC, it can still cover a wide range of ADC values with reasonable accuracy. Consequently, when such a scheme is compared with the two schemes A and B (with the same total number of DW acquisitions), one would expect that it will have not only better noise performance (its index value is smaller than either A or B), but also it will be able to delineate anisotropic structures with orientational variability (as it is the case in brain) more efficiently than either scheme A or B. In the published DTI literature, DTI measurement using multiple DW gradient directions (more than the commonly used six or seven) has been reported only once (40) (using 12 DW gradient directions), but no further details were given about the definition of the applied scheme.

The theoretical analysis and the experiments in this study made two simplifying assumptions:

(a) They neglected the effect of the imaging gradients on the $\mathscr{B}$ matrix. The DW pulse sequence for the experiments was designed so as to refocus the imaging gradients as soon as possible after their application (19, 26). The very good approximation of the measured isotropic tensor for each scheme, derived by the phantom experiments, verified that the imaging gradients exerted negligible effect on $\mathscr{B}$.

(b) They assumed the SNR of the common baseline signal (SNR_0) was identical in the different DTI schemes, and therefore, they ignored the effect of the distribution of a given DW gradient strength among the three Cartesian gradient directions on the noise performance of the DTI schemes. For example, in order to achieve a DW gradient magnitude G_m, scheme A required 0.707 times the maximum gradient magnitude G_m at each Cartesian gradient direction, while scheme B required the full maximum gradient magnitude G_m. Treating both implementations as equivalent obviously leads to a suboptimal use of the gradient capabilities for scheme A, since it uses only 70.7% of the gradient output used by either scheme B or 12.

The results from the simulations and the phantom experiments established that the index κ was proportional to the total variance of $\mathbf{D}$ of an isotropic medium, when all the DW acquisitions use the same b value. It was shown that implementation of the two schemes A and B using a single b value for multiple DW acquisitions per DW gradient direction leads generally to increased error in the estimation of $\mathbf{D}$ for anisotropic cases, when compared to the imple-

mentation of the schemes, using different b values for multiple DW acquisitions per DW gradient direction. Furthermore the simulations showed that for each DTI scheme, the total variance of $\mathbf{D}$ is always higher for anisotropic fibers than for isotropic ones. Nevertheless, scheme 12 showed the weakest noise dependence on the degree of anisotropy, while scheme B showed the strongest. In addition, the relative differences in noise performance of the three schemes became more pronounced when the degree of anisotropy increased.

Both those results lead to the conclusion that the physical quantity corresponding to the index κ evaluates the noise performance of a DTI scheme under the most favorable conditions. Consequently, for schemes with an index value relatively far from the optimum, such as scheme B, we would expect the effect of noise for increased levels of anisotropy to become increasingly more prominent than the one for DTI schemes with an index value relatively close to the optimum, such as scheme A. In any case, the proposed scheme 12 gave the smallest errors and showed the smallest dependence of noise on the degree of diffusion anisotropy.

Although the mean diffusivity maps derived from the DTI human brain experiments had predominantly similar appearances for the three compared schemes, the respective anisotropy maps revealed significant differences in the noise appearance, in qualitative agreement with the difference in the index values of the schemes. Consequently, schemes A and B can under no circumstances be treated as equivalent: scheme A yields better quality DTI measurements than scheme B. In addition, scheme 12, derived from the index optimization with 12 DW acquisitions, yielded measurements of the best quality among the compared schemes.

We thus conclude that we have developed a systematic method for the evaluation of the effect of the DW gradient directions employed by a DTI acquisition schemes on the noise performance of the scheme. The method leads also to the definition of new schemes, which can sample the space of the effective diffusion ellipsoid densely and uniformly, improving thus the noise performance of the final results of the DTI measurements.

ACKNOWLEDGMENTS

REFERENCES

1. P. J. Basser, J. Mattiello, and D. Le Bihan, MR diffusion tensor spectroscopy and imaging. *Biophys. J.* **66**, 259–267 (1994).

2. P. J. Basser, J. Mattiello, and D. Le Bihan, Estimation of the effective self-diffusion tensor from the NMR spin echo. *J. Magn. Reson. B* **103,** 247–254 (1994).

3. A. M. Ulug, P. B. Barker, R. N. Bryan, and P. C. M. van Zijl, Diffusion tensor imaging of the human brain, *in* "Proceedings: SMR Third Scientific Meeting, Nice, France," p. 901, Berkeley, CA (1995).

4. C. Pierpaoli, P. Jezzard, and P. J. Basser, High resolution diffusion tensor imaging of the human brain, *in* "Proceedings: SMR Third Scientific Meeting, Nice, France," p. 899, Berkeley, CA (1995).

5. T. G. Reese, R. M. Weisskoff, R. N. Smith, B. R. Rosen, R. E. Dinsmore, and V. J. Wedeen, Imaging myocardial fiber architecture in vivo with magnetic resonance. *Magn. Res. Med.* **34,** 786–791 (1995).

6. M. R. Drost, C. C. van Donkelaar, L. J. G. Kretzers, and K. Nicolay, A comparison of local muscle fibre direction measured by diffusion tensor imaging (DTI) with muscle fibre direction as determined in an actual section, *in* "Proceedings: ISMRM Fifth Scientific Meeting, Vancouver BC, Canada," p. 1717, Berkeley, CA (1997).

7. E. J. Chiu, J. C. Lotz, and S. Majumdar, Diffusion tensor imaging applied to the human intervertebral disc in vitro, *in* "Proceedings: ISMRM Fourth Scientific Meeting, New York, NY," p. 1319, Berkeley, CA (1996).

8. C. Pierpaoli and P. J. Basser, Towards a quantitative assessment of diffusion anisotropy. *Magn. Reson. Med.* **36,** 893–906 (1996).

9. C. Pierpaoli, P. J. Jezzard, P. J. Basser, and A. Barnett, Diffusion tensor MR imaging of the human brain. *Radiology* **201,** 637–648 (1996).

10. D. J. Werring, C. A. Clark, G. J. M. Parker, G. J. Barker, M. R. Symms, F. Franconi, D. H. Miller, and A. J. Thompson, Exploring links between brain structure and function: Combining diffusion tensor imaging (DTI) with functional magnetic resonance imaging (fMRI), *in* "Proceedings: ISMRM Sixth Scientific Meeting, Sydney, Australia," p. 1497, Berkeley, CA (1998).

11. A. G. Sorensen, R. G. Gonzalez, R. M. Weisskoff, T. L. Davis, T. G. Reese, W. A. Copen, J. L. Boxerman, J. P. Sasson, and B. R. Rosen, In vivo full diffusion tensor measurement in normal and pathologic human brain, *in* "Proceedings: ISMRM Fourth Scientific Meeting, New York, NY," p. 1327, Berkeley, CA (1996).

12. H. L. Lutsep, G. W. Albers, A. DeCrespigny, G. N. Kamat, M. P. Marks, and M. E. Moseley, Clinical utility of diffusion-weighted magnetic resonance imaging in the assessment of ischemic stroke. *Ann. Neurol.* **41,** 574–580 (1997).

13. D. K. Jones, S. C. R. Williams, A. Simmons, P. M. W. Bath, H. S. Markus, G. R. Cherryman, and M. A. Horsfield, The nature of chronic ischaemic damage and lacunar infarction demonstrated by diffusion tensor MRI, *in* "Proceedings: ISMRM Fifth Scientific Meeting, Vancouver, BC, Canada," p. 1712, Berkeley, CA (1997).

14. A. L. Tievsky, T. Ptak, O. Wu, J. Farkas, R. G. Gonzalez, B. R. Rosen, and A. G. Sorensen, Evaluation of MS lesions with full tensor diffusion weighted imaging and anisotropy mapping, *in* "Proceedings: ISMRM Fifth Scientific Meeting, Vancouver BC, Canada," p. 901, Berkeley, CA (1997).

15. C. Y. Tang, S. Peled, M. S. Buchsbaum, Gudbjartsson, D. Lu, J. Downhill, M. Haznedar, E. A. Hazlett, and S. W. Atlas, Correlates between glucose metabolic rate and diffusion anisotropy in normals and schizophrenics, *in* "Proceedings: ISMRM Fifth Scientific Meeting, Vancouver, BC, Canada," p. 665, Berkeley, CA (1997).

16. C. Pierpaoli, A. Barnett, T. Penix, L. De Graba, P. J. Basser, and J. Di Chiro, Identification of fiber degeneration and organized gliosis in stroke patients by diffusion tensor MRI, *in* "Proceedings: ISMRM Fourth Scientific Meeting, New York, NY," p. 563, Berkeley, CA (1996).

17. A. Simmons, A. Darekar, D. K. Jones, M. A. Horsfield, T. S. Cox, M. A. Jeffree, and S. C. R. Williams, Diffusion tensor MRI applied to intra-axial brain tumours, *in* "Proceedings: ISMRM Sixth Scientific Meeting, Sydney, Australia," p. 1636, Berkeley, CA (1998).

18. P. J. Basser and C. Pierpaoli, Microstructural and physiological features of tissues elucidated by quantitative diffusion tensor MRI. *J. Magn. Reson. B* **111,** 209–219 (1996).

19. J. Matiello, P. J. Basser, and D. Le Bihan, Analytical expressions for the b matrix in NMR diffusion imaging and spectroscopy. *J. Magn. Reson. A* **108,** 131–141 (1994).

20. E. O. Stejskal and J. E. Tanner, Spin diffusion measurements: Spin-echoes in the presence of a time-dependent field gradient. *J. Chem. Phys.* **42,** 288–292 (1965).

21. D. Le Bihan, E. Breton, D. Lallemand, P. Grenier, E. Cabanis, and M. Laval-Jeantet, MR imaging of intravoxel incoherent motions. Applications to diffusion and perfusion in neurologic disorders. *Radiology* **161**(2), 401–407 (1986).

22. W. H. Press, B. P. Flannery, S. A. Teukolsky, and W. T. Vetterling, "Numerical Recipes in C: The Art of Scientific Computing," 2nd ed., Cambridge University Press, Cambridge (1992).

23. P. R. Bevington, "Data Reduction and Error Analysis for the Physical Sciences," 2nd ed., McGraw-Hill, New York (1992).

24. D. G. Taylor and M. C. Bushell, The spatial mapping of translational diffusion coefficients by the magnetic resonance imaging technique. *Phys. Med. Biol.* **30,** 345–349 (1985).

25. K. D. Merbolt, W. Hanicke, and J. Frahm, Self-diffusion NMR imaging using stimulated echoes. *J. Magn. Reson.* **64,** 479–486 (1985).

26. J. Matiello, P. J. Basser, and D. Le Bihan, The b matrix in diffusion tensor echo-planar imaging. *Magn. Reson. Med.* **37,** 292–300 (1997).

27. D. Xing, N. G. Papadakis, C. L. H. Huang, V. M. Lee, T. A. Carpenter, and L. D. Hall, Optimized diffusion-weighting for measurement of apparent diffusion coefficient (adc) in human brain. *Magn. Reson. Imaging* **15,** 771–784 (1997).

28. B. J. Fisher, N. Dillon, A. A. Wilkinson, T. A. Carpenter, and L. D. Hall, Design and evaluation of a transverse gradient set for magnetic resonance imaging of the human brain. *Meas. Sci. Technol.* **7,** 838–843 (1996).

29. C. E. Hayes, W. A. Edelstein, J. F. Shenck, O. M. Mueller, and M. Eash, An efficient, highly homogeneous radiofrequency coil for whole-body NMR imaging at 1.5 T. *J. Magn. Reson.* **63,** 622–628 (1985).

30. R. Turner and D. Le Bihan, Single-shot diffusion imaging at 2.0 Tesla. *J. Magn. Reson.* **86,** 445–452 (1990).

31. M. S. Cohen and R. M. Weisskoff, Ultra-fast imaging. *Magn. Reson. Imaging* **9,** 1–37 (1991).

32. P. W. Atkins, "Physical Chemistry." 4th ed., Oxford University Press, Oxford (1990).

33. E. M. Haacke, E. D. Lindskog, and W. Lin, A fast, iterative, partial-Fourier technique capable of local phase recovery. *J. Magn. Reson.* **92,** 126–145 (1991).

34. D. Le Bihan, E. Breton, D. Lallemand, M. L. Aubin, J. Vignaud, and M. Laval-Jeantet, Separation of diffusion and perfusion in intravoxel incoherent motion MR imaging. *Radiology* **168**(2), 497–505 (1988).

35. R. Turner, D. Le Bihan, J. Maier, R. Vavrek, L. K. Hedges, and J.

Pekar, Echo planar imaging of intravoxel incoherent motion. *Radiology* **177,** 407–414 (1990).

36. R. L. Ehman and J. P. Felmlee, Adaptive technique for high-definition MR imaging of moving structures. *Radiology* **173,** 255–263 (1989).

37. R. J. Ordidge, J. A. Helpern, Z. X. Qing, R. A. Knighr, and A. Nagesh, Correction of motional artifacts in diffusion-weighted MR images using navigator echoes. *Magn. Reson. Imaging* **12,** 455–460 (1994).

38. A. W. Anderson and J. C. Gore, Analysis and correction of motion artifacts in diffusion weighted imaging. *Magn. Reson. Med.* **32,** 379–387 (1994).

39. P. Webb and A. Macovski, Rapid, fully automatic, arbitrary-volume in vivo shimming. *Magn. Reson. Med.* **20,** 113–122 (1990).

40. C. Pierpaoli, Oh no! One more method for color mapping of fiber tract direction using diffusion MR imaging data, *in* "Proceedings: ISMRM Fifth Scientific Meeting, Vancouver BC, Canada," p. 1741, Berkeley, CA (1997).